Negative mass density and ρ-near-zero quasi-two-dimensional metamaterials: Design and applications

Rogelio Graciá-Salgado, Victor M. García-Chocano, Daniel Torrent, and José Sánchez-Dehesa[*]

Wave Phenomena Group, Universitat Politècnica de València, Camino de Vera s.n. (Building 4D), ES-46022 Valencia, Spain

We report the design and the characterization of artificial structures made of periodical distributions of structured cylindrical scatterers embedded in a two-dimensional (2D) waveguide. For certain values of their geometrical parameters they show simultaneously negative effective bulk modulus and negative effective mass density. Here our analysis is focused on the frequencies where they behave like materials with negative density or density near zero (DNZ). The scattering units consist of a rigid cylindrical core surrounded by an anisotropic shell divided in angular sectors. The units are embedded in a 2D waveguide whose height is smaller than the length of the cylinders, which makes the structure quasi-2D. We have obtained the dispersion relation of the surface acoustic waves excited at frequencies with negative effective density. Also, we report phenomena associated with their DNZ behavior, such as tunneling through narrow channels, control of the radiation field, perfect transmission through sharp corners, and power splitting. Preliminary experiments performed on samples with millimeter-scale dimensions demonstrated their single-negative behavior, with the main drawback being the strong losses measured at the frequencies where the negative behavior is observed.

I. INTRODUCTION

Acoustic metamaterials are artificial structures with acoustic properties not found in natural materials. These structures are essentially periodic composites of subwavelength units which present an unusual macroscopic behavior as a whole. The resulting properties can be exploited for giving rise to many interesting acoustic devices, which have been already reported in review articles and books.[1,2] For example, metamaterials with dynamical mass anisotropy have been applied to develop hyperlenses,[3] gradient index lenses,[4,5] subwavelength resonators,[6] radial acoustic crystals,[7,8] acoustic cloaks,[9,10] and many other devices proposed within the framework of transformation-based solutions.[11–13]

Acoustic metamaterials are mainly known because of their behavior as acoustic structures with negative bulk modulus,[14–17] negative mass density,[18–21] or both simultaneously.[22–28] These fascinating behaviors appear at narrow frequency bands and their physical origin has been explained in terms of the internal resonances of the building units:[22] the negative bulk modulus being associated with monopolar resonances while the negative density is associated to dipole-type resonances.

Negative bulk modulus has been demonstrated by using quasi-one-dimensional arrays of Helmholtz resonator embedded in water[14] and in air.[15,16] More recently, quasi-two-dimensional structures exhibiting negative bulk modulus have been demonstrated by using boreholes drilled in a two-dimensional (2D) waveguide.[17] On the other hand, the dipolar resonances appear when using structured units consisting of a heavy mass core surrounded by a soft polymer, both being embedded in a relatively rigid epoxy.[18] Currently, the usual approach is based on one-dimensional (1D) arrays of elastic membranes,[19–21] the main drawback being the high degree of precision required for the tension applied to the membranes, which must be the same. This issue has been overcome in a recent proposal,[29] where the negative density behavior is obtained in a 2D waveguide with a periodic distribution of cavities filled up with an isotropic metafluid, its sound speed being smaller than that of the surrounding background. This condition is easy to engineer, as has been already demonstrated.[30] The proposed structures are robust and present double negative behavior at frequency regions which can be tailored by adjusting the cavity parameters.

In this work we report the characterization of quasi-2D artificial structures behaving as double negative acoustic materials in certain frequency regions and that can be used as density-near-zero (DNZ) materials in selected frequencies. These structures consist of anisotropic cylindrical scatterers penetrating in one of the rigid walls defining the 2D acoustic waveguide. In other words, the length of the scattering units exceeds the height of the waveguide in such a manner that they can be referred to as quasi-2D sonic crystals. These structures are different than others reported since the DNZ behavior does not involve the use of membranes or the presence of an additional fluid inside each scatterer. Therefore, the proposed structures are easily fabricated using any material with acoustic impedance much higher than that of the surrounded background, which will be air in the present work.

The article is organized as follows. After this Introduction, in Sec. II, the proposed structure is studied in the low-frequency limit and the effective parameters of the resulting metamaterial are obtained by solving the scattering problem. In the following sections we report several numerical experiments based on the finite elements method (FEM), showing several applications of these metamaterials. Particularly, Sec. III shows that the excitation of surface acoustic waves is possible, which opens the possibility of the amplification of evanescent waves and acoustic superlensing. Section IV analyzes several applications of these metamaterials working at the frequencies where the structure shows a DNZ behavior. The tunneling through narrow channels, the tailoring of the radiation pattern, and the transmission through sharp bends and the power
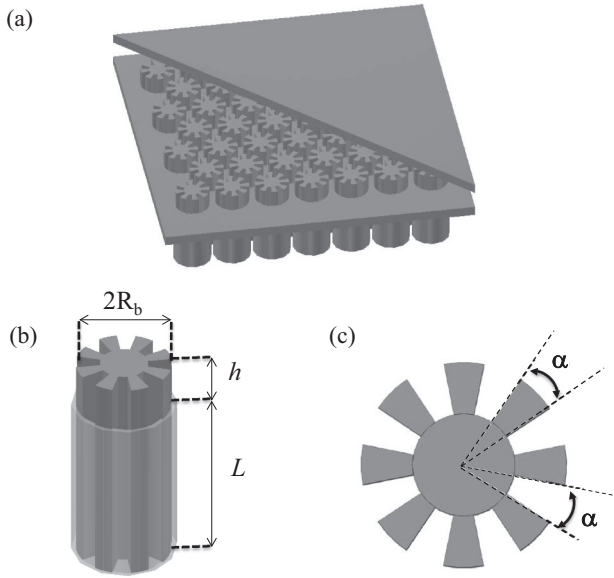
FIG. 1. (a) Schematic view of the structure under study. It is made of an array of anisotropic scatterers embedded in a 2D waveguide with height h. (b) Scheme of an individual scatterer consisting of a structured cylinder with radius R_b and total length $L + h$, where L is length extending into the 2D waveguide. The wall is made semitransparent to observe that corrugations extend along the whole length L. (c) Section of the scatterer showing its angular anisotropy. The grayed regions represent an acoustically rigid material.

distribution among several waveguides are discussed through simulations based on FEM. The transmission spectra of two fabricated structures are described in Sec. V. Finally, the work is summarized in Sec. VI. The Appendix describes the mathematical procedure to obtain the T matrix of the proposed structures.

II. ACOUSTIC METAMATERIAL: EFFECTIVE PARAMETERS

Figure 1(a) shows a schematic view of the proposed metamaterial. It consists of a periodic array of cylindrical scatterers embedded in a 2D waveguide, which is defined by two infinite parallel rigid planes separated by a distance h. The structure of a single scatterer is shown in Fig. 1(b). Note that the total length of the cylindrical scatterer is $L + h$, L being the part inserted in the bottom plane of the 2D waveguide. R_b is the external radius of the cylinder and R_a is the radius of the internal core that is an acoustically rigid cylinder. The space between the rigid core and the external radius is angularly partitioned into equal sectors, as it is depicted in Fig. 1(c). Note that the resulting system is defined with five parameters (i.e., h, R_a, R_b, L, and α), with which the acoustics properties can be totally controlled.

In what follows we show that an isolated unit is able to maintain monopolar and dipolar resonances in separated frequency regions. This property justifies its use as the building unit of metamaterials with negative parameters (see Sec. II A).

A. Effective acoustic parameters of the scattering unit: $B_a(\omega)$ and $\rho_a(\omega)$

The frequency-dependent bulk modulus and dynamic mass density $B_a(\omega)$ and $\rho_a(\omega)$, respectively, of the scattering units are[31]

$$\frac{B_a(\omega)}{B_b} = \frac{k_b^2 R_b^2}{2} \ln k_b R_b - \frac{1}{2} k_b R_b \chi_0, \tag{1}$$

$$\frac{\rho_a(\omega)}{\rho_b} = \frac{\chi_1}{k_b R_b}, \tag{2}$$

where B_b and ρ_b are the background parameters and $k_b = \omega/c_b$ the corresponding wave number. In this work, the fluid background under consideration is air with density $\rho_b = 1.25$ kg/m^3 and sound speed $c_b = 343$ m/s.

The quantities χ_0 and χ_1 are related with the two first diagonal elements T_0 and T_1, respectively, of the T matrix describing this scattering unit. It has been shown that[31]

$$T_q = -\frac{\chi_q \dot{J}_q(k_b R_b) - J_q(k_b R_b)}{\chi_q \dot{H}_q(k_b R_b) - H_q(k_b R_b)}, \tag{3}$$

where J_q and H_q are the qth-order Bessel and Hankel functions, respectively, and the dot top indicates the partial derivative with respect to their argument.

The solutions for χ_0 and χ_1 inserted in Eqs. (1) and (2) allow the calculation of the frequency-dependent parameters, $B_a(\omega)$ and $\rho_a(\omega)$. A typical behavior of these parameters for a given geometry is shown in Fig. 2, where it is shown how the frequency response is complex due to the oscillations of the pressure field inside the structured unit. These oscillations appear, as in the case of the units based on an isotropic fluid,[29] because of the smaller sound speed inside the scattering unit in comparison with that in the background. Note that the proposed cylindrical scatter enters a length L inside one surface of the 2D waveguide, so that the scatterer presents a dynamical mass density apparently smaller than that of the background by a
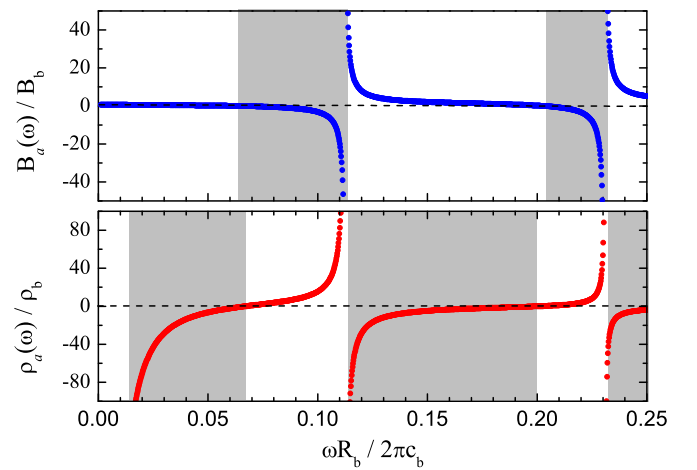
FIG. 2. (Color online) Effective bulk modulus (top panel) and effective mass density (bottom panel) as a function of the frequency (in reduced units) corresponding to the scattering unit depicted in Fig. 1. The parameters are $h = R_b$, $L = 3.5h$, $R_a = 0.5R_b$, and $\alpha = \pi/8$. The shadowed areas define the frequencies where the acoustic parameters have negative values.

factor $\approx h/L$. Also, the presence of the rigid sectors in the shell surrounding the central core forbids the propagation of sound along the angular direction, having an effect of reduction in the sound speed, as has been shown in Ref. 6.

The existence of a frequency region where the structure shows a negative bulk modulus is due to the length L of the cavity, which acts as a Helmholtz resonator, as has been widely demonstrated.[14–17] Regarding the behavior for the mass density at very low frequencies, we do not expect an infinite negative mass extending up to zero frequency. The results for frequencies close to zero are not displayed since the analytical model in Eq. (2) contains approximations that give unreliable values for extremely low frequencies.

B. Effective parameters of the acoustic metamaterial: $B_m(\omega)$ and $\rho_m(\omega)$

Let us consider now the periodic structure depicted in Fig. 1(a), which consists of a hexagonal distribution of the scattering units shown in Fig. 1(b). For wavelengths larger than the lattice constant, a, this structure behaves as an effective medium with some frequency-dependent effective mass density $\rho_m(\omega)$ and bulk modulus $B_m(\omega)$, which can be obtained from $B_a(\omega)$ and $\rho_a(\omega)$ using the relationships[31]

$$\frac{1}{B_m(\omega)} = \frac{1-f}{B_b} + \frac{f}{B_a(\omega)}, \qquad (4)$$

$$\rho_m(\omega) = \frac{(1+f)\rho_b + (1-f)\rho_a(\omega)}{(1-f)\rho_b + (1+f)\rho_a(\omega)}, \qquad (5)$$

where f is the filling fraction of the underlying lattice. For the hexagonal lattice, $f = (2\pi/\sqrt{3})(R_b/a)^2$.

A comprehensive analysis of the values taken by these parameters as a function of the six parameters defining the structure (h, R_a, R_b, L, α, and a) is a cumbersome task and it is beyond the scope of this work. We have here reduced the analysis to two cases that we consider of interest.

We have simplified our study to structures made of scattering units with parameters $R_a = 0.5R_b$, $L = 3.5h$, and $h = R_b = 0.44a$. It should be pointed out that the central core considered here (with radius $R_a \neq 0$) not only adds an additional degree of freedom into the design of the metamaterial, but also has practical benefits; sharp corners are avoided which, in principle, diminishes dissipation losses. First, we looked for the frequencies with negative values of the acoustic parameters as a function of L/h, the ratio between the length L and the height h of the 2D waveguide.

Figure 3 shows the results of our study represented in a phase diagram plot; the area enclosed by the continuous (dashed) lines represent the regions where the effective mass density (effective bulk modulus) is negative. Frequencies are only represented below the homogenization limit, which is 0.25 (in reduced units). In terms of wavelengths $\lambda \geqslant 4a$ (Ref. 30). Note that negative density starts appearing for ratios $L/h \geqslant 0.78$. Above this point, the reduction of the effective density in a single scatterer is larger enough to produce a metamaterial with negative dynamical mass density. Figure 3 also indicates that it is not until L/h larger than 2 where the cavity length L is large enough to act as a Helmholtz
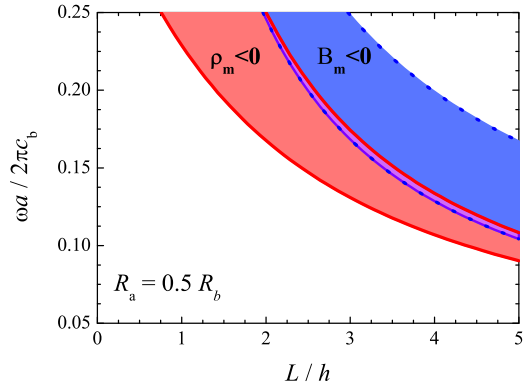
FIG. 3. (Color online) Colored areas define the values $\omega - L/h$, where the metamaterial parameters are negative. The small overlapping region between them gives the conditions where both parameters are simultaneously negative. These results are obtained using the structure depicted in Fig. 1, with parameters $h = R_b$ and $\alpha = \pi/8$.

resonator and, therefore, produce a metamaterial with negative bulk modulus. It is observed that with increasing values of the ratio L/h, the corresponding frequencies with negative values shift to lower frequencies, where the homogenization limit is even more accurate.

In comparison with analogous structures based on arrays of isotropic metafluid shells[32] the overlap between negative regions is now produced in a narrow strip of frequencies. This result is due to the large frequency separation between the resonances associated with the effective bulk modulus and the mass density, respectively, as shown in Fig. 2. Also remember that single-negative values in Fig. 3 correspond to imaginary values of the metamaterial sound speeds c_m. Effectively, since $c_m = \sqrt{B_m/\rho_m}$, there will be no propagation through the metamaterial and a band gap exists in the acoustic band structure of the infinite periodic system.

A typical example of the frequency dependence of the effective parameters is depicted in Fig. 4, which is a cut along the line $L = 3.5R_b$ in the phase diagram shown in Fig. 3. A narrow frequency region can be observed, located in the interval [0.146-0.151], where both parameters are simultaneously negative. The double negativity behavior is a very interesting phenomenon in all types of metamaterials but it is especially challenging for airborne propagation, where the possibilities of having resonant structures is limited due to the scarce interaction of sound waves with solid structures.

Figure 5 represents the second case of interest. Now, the phase diagram of the same structure is shown when the cavity length is kept constant and the negative behavior is analyzed as a function of the ratio R_a/R_b. As before, the continuous lines enclose the areas with negative dynamical mass density while the dotted line encloses the area with negative bulk modulus. Note that the influence of the central core (R_a) is weak for values of $R_a/R_b \leqslant 0.4$, which means that in the fabrication process this cylinder will not affect the global behavior of the metamaterial. Above this value, the narrowing of the negative regions begins until they completely disappear at $R_a \approx R_b$, where the scattering units become acoustically rigid cylinders.
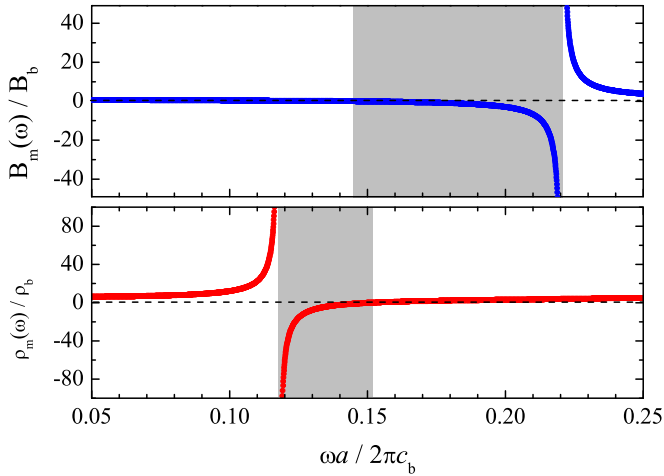
FIG. 4. (Color online) Frequency dependence of the effective bulk modulus and dynamical mass density for the structure depicted in Fig. 1(a). The results correspond to the case with geometrical parameters $h = R_b = 0.44a$, $R_a = 0.5R_b$, $\alpha = \pi/8$, and $L = 3.5h$. The shadowed areas correspond to the frequencies with negative values.

III. NEGATIVE DYNAMICAL MASS: SURFACE ACOUSTIC WAVES

Acoustic metamaterials with negative dynamical mass density have been experimentally demonstrated using soft rubber spheres in water[18] or employing lattices of membranes in air.[19,21] The negative value is obtained thanks to the dipole-type resonances exhibited by the building units forming the metamaterial. These dipole-type resonances produce that the response of the fluid—acceleration—be out of phase with the dynamic pressure gradient.[22] However, it has been pointed out that metamaterials based on membranes present several drawbacks, like repeatability of the building units or aging of the materials. Thus, different approaches should be explored in order to propose robust structures with the same negative behavior in the dynamical density.
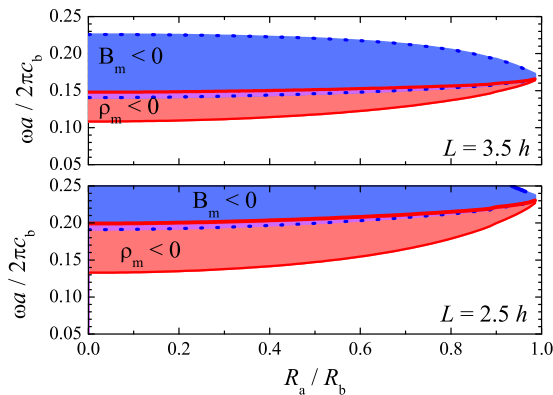
FIG. 5. (Color online) Area enclosed by the continuous (dashed) lines gives the values $\omega - R_a/R_b$ where the dynamical mass density (bulk modulus) is negative. The overlapping area defines the zones where double negative parameters are produced.

Amplification of evanescent waves has been experimentally demonstrated using membrane-based 2D metamaterials slabs.[21] In a similar manner, this section demonstrates that the amplification is also possible using our quasi-2D structures working at the frequencies with negative effective density. The amplification of evanescent modes was theoretically proposed in acoustics by Ambati and co-workers[33] following the analogous result obtained for EM waves provided by slabs of negative-permittivity materials.

Let us consider the simple case in which we have an interface between two semi-infinite mediums: Medium I is the air background with positive mass and modulus, whereas medium II is the metamaterial under study with mass density ρ_m and bulk modulus B_m. The wave vectors in these media are, respectively,

$$k_b = \sqrt{k_{b,x}^2 + k_{b,y}^2}, \tag{6}$$

$$k_m = \sqrt{k_{m,x}^2 + k_{m,y}^2}, \tag{7}$$

where $k_{i,x}$ and $k_{i,y}$ are the Cartesian components of the wave vector k_i $(i = b,m)$, being $k_{b,y} = k_{m,y} = k_y$ because of the continuity of the parallel wave vectors at the air-metamterial interface. Figure 6 shows the schematic view of the physical system under study, where the metamaterial slab with thickness D is embedded in a fluid background (air in this work).

The matching of the pressure and normal velocity at the interface gives the relation between the normal components of the respective wave vectors:[33]

$$\frac{k_{b,x}}{\rho_b} + \frac{k_{m,x}}{\rho_m(\omega)} = 0. \tag{8}$$

Since the necessary condition for having a bound state at the air-metamaterial interface is that both $k_{b,x}$ and $k_{m,x}$ have
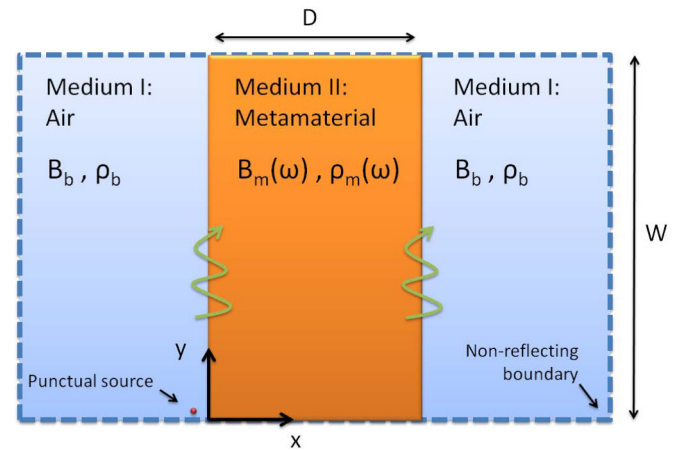
FIG. 6. (Color online) Scheme of the computational setup employed in the finite element simulations. The multilayered system air-metamaterial-air is enclosed in a domain with nonreflective boundaries. A punctual source is placed in the left air layer, at the bottom right corner near the metamaterial slab, in order to excite surface modes along each interface.

positive imaginary parts, it is concluded from Eq. (8) that $\rho_m(\omega)$ must be negative.

A numerical experiment has been performed through a 3D FEM simulation using a slab made of nine rows of cylinders distributed in a square lattice with lattice period a and a length of $W = 17a$. Figure 6 depicts the computational domain which considers that all the external boundaries are reflectionless interfaces which absorb the outgoing waves. In order to excite the surface states, a point source has been placed in the air near the metamaterial surface. The square lattice is here preferred due to plotting advantages; the pressure field can be easily depicted along an axis passing between the two consecutive rows of scatterers. For this lattice, the filling ratio is $f = \frac{\pi R_b^2}{a^2}$. The slab has been enclosed in a waveguide with rigid walls of height $h = 0.47a$. The values of parameters describing the scatterers are (see Fig. 3) $L = 1.65a$ ($L = 3.5h$). For these values the negative mass behavior appears within the range $\omega a/2\pi c \in [0.105, 0.135]$.
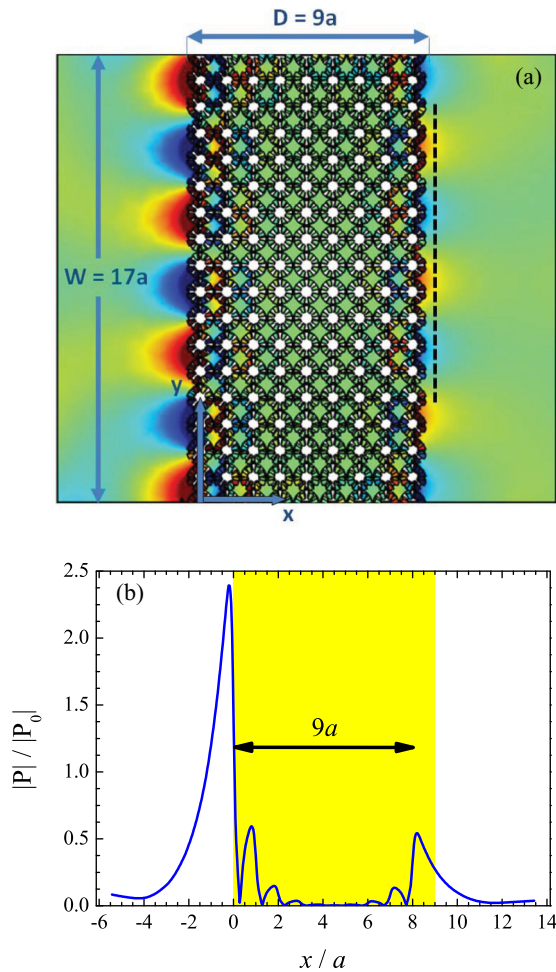
FIG. 7. (Color online) (a) Surface waves excited at the air-metamaterial interface using a punctual source emitting at the frequency 0.122 (in reduced units). The vertical dashed line corresponds to the zone where the pressure field is processed in order to determine the dispersion relation of the surface modes. (b) Normalized pressure amplitude of the evanescent waves along the x direction. It is calculated at the equatorial plane between two rows of scatterers.

Figure 7(a) shows a snapshot of the pressure amplitude excited with the source radiating at $\omega a/2\pi c = 0.122$. It is observed that surface acoustic waves are generated in both air-metamaterial interfaces. The amount of this effect is better displayed in Fig. 7(b), where the dependence of the amplitude profile is shown along the horizontal x axis for the value $y = 8.5a$. This figure shows that the amplitude is maximum at the interface where the source is located and it decreases to the right, as expected. However, note that inside the metamaterial the envelope of the amplitude decreases towards the interior until it reaches the center, where it starts increasing up to the opposite interface. The maxima observed under the envelope are due to the excitation of the local resonances in the scattering elements producing a field accumulation inside them. This accumulation is smaller for deeper positions inside the slab.

The increasing of pressure amplitude in the opposite interface is due to the fact that the conditions for the existence of a propagating surface acoustic wave are accomplished. Therefore, since the metamaterial thickness is small enough, the coupling between both surface states is possible and the excitation at one interface allows the excitation at the other one. The behavior here described is similar to that experimentally observed by Park *et al.*,[21] who used a square distribution of membranes embedded in a 2D waveguide with $h = 5$ mm. Therefore, we can conclude that the possibility of acoustic superlensing should be possible by using our artificial structures if the losses associated to the dipole-type resonances are small enough.

The dispersion relation of the surface states has been obtained from the data obtained from the numerical experiment. The vertical wave vector of these modes k_y was calculated by determining their wavelength along the y axis at each frequency. This task was performed through a Fourier transform of the pressure field evaluated along the dashed line in Fig. 7(a), which is parallel to the air-metamaterial interface for $x = 9a$. The response obtained is the same for the two isotropic lattices in 2D (i.e., for the hexagonal and square lattices) and it is represented with symbols in Fig. 8. The continuous line in this figure corresponds to the dispersion relation resulting from the theoretical model,[33]

$$k_y^2(\omega) = \frac{\omega^2}{c_b^2} \frac{\rho^*(\omega)}{1 - \rho^*(\omega)^2} \left[\rho^*(\omega) - \frac{1}{B^*(\omega)} \right], \quad (9)$$

where

$$\rho^* = \frac{\rho_m}{\rho_b}, \quad B^* = \frac{B_m}{B_b}. \quad (10)$$

It is observed in Fig. 8 that the dispersion relation of the surface waves is similar to that of the surface plasmons. Since they are localized, they appear at frequencies below the "light" line $\omega = c_b k_b$, which is represented by the black dashed line in Fig. 8. This figure also shows a small shift between the data obtained from the FEM simulations and those obtained by the analytical model. This deviation is due to the fact that the theoretical approach assumes an approximation when considering a coefficient of anisotropy $\gamma = 0$ (see Appendix A). For the highest frequencies, large values of k_y lead to small wavelengths along the y axis and, consequently, the structure no longer behaves as an uniform medium. This fact leads to the unphysical (spurious) points
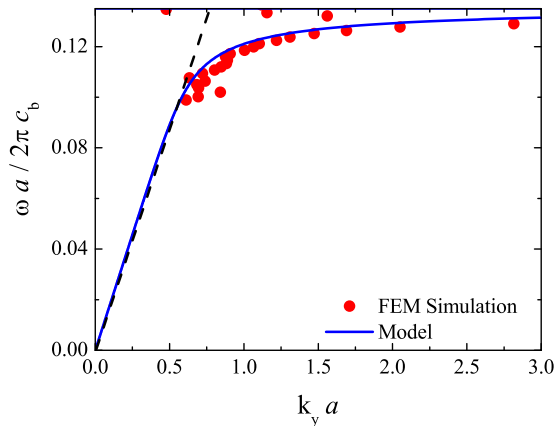
FIG. 8. (Color online) Dispersion relation of the surface states obtained at the air-metamaterial interface, where the metamaterial consists of an isotropic lattice (hexagonal or square) of the cylindrical units shown in Fig. 1. The parameter's values of the structured cylinders are $R_a = 0.5R_b$, $\alpha = \pi/8$, and $R_a = h = 0.47a$, where a is the lattice constant. The continuous line represents the result obtained using the mode-matching method while the symbols are results obtained from 3D simulations based on FEM. The black dashed line represents the line describing the propagation in the air background $\omega = c_b k_b$.

observed in Fig. 8. Note the overall good agreement between the theoretical model and the FEM simulations. These results give support to the theory here developed and confirm that the structures proposed in this work exhibit negative mass density.

IV. APPLICATIONS OF DNZ METAMATERIALS

The EM counterpart of DNZ acoustic metamaterials are those with low permittivity or ϵ-near-zero (ENZ) materials, which have been proposed for a rich variety of applications, like cloaking,[34,35] "squeezing" and tunneling of EM waves through very narrow channels,[36–38] and radiation patterning.[39] Since all these amazing phenomena are basically exploiting the condition of infinite phase velocity of EM waves occurring with ENZ materials, similar behaviors are expected for acoustic waves when working with DNZ metamaterials.

In this section we report FEM simulations showing that the artificial structures here introduced can be employed to develop similar applications at the frequencies where DNZ is obtained. In particular, the tunneling through narrow channels, the transmission through sharp bends and the filtering of transverse modes due to radiation patterning are theoretically demonstrated. Results is this section are obtained using the same geometrical parameters from the previous sections.

A. Tunneling of acoustic waves through narrow channels

An exciting application of our DNZ acoustic metamaterial is the possibility of squeezing the major portion of the 2D propagating sound energy into an ultranarrow channel filled with it, like it has been recently demonstrated in its EM counterpart.[37,38] As in the case for EM waves, the phenomenon can be explained in terms of the effective infinity phase velocity inside the DNZ metamaterial. In brief, since $c_m = \sqrt{\frac{B_m}{\rho_m}}$, for
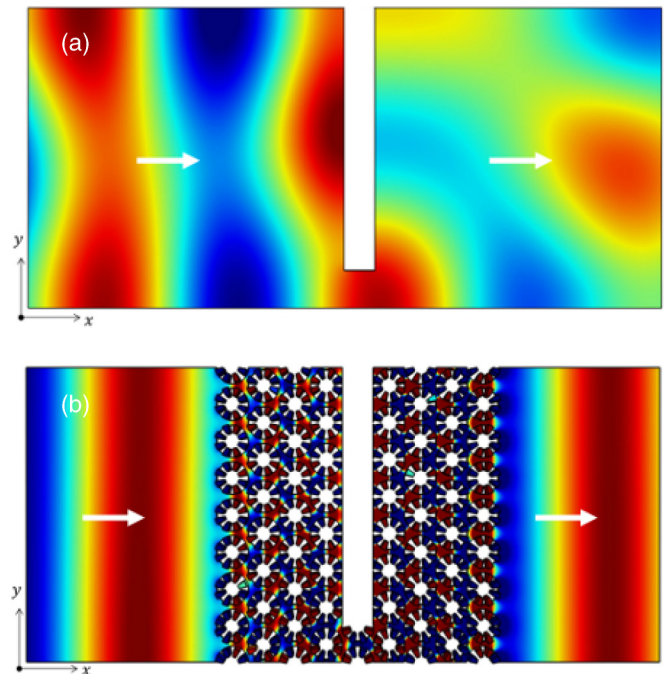
FIG. 9. (Color online) (a) Pressure map showing the sound propagation through a narrow channel. The white strip represents a rigid wall. (b) Resulting map when the channel is embedded in a DNZ metamaterial slab made of the scatterers depicted in Fig. 1. The white arrows indicate the direction of wave propagation.

the selected frequencies where $\rho_m \approx 0$, then $c_m \to \infty$ and consequently the wave vector inside the metamaterial $k_m = \omega/c_m \to 0$, which implies that the phase of the wave does not advance while the sound propagates inside the metamaterial. Note that reflections are avoid at the air-metamaterial interface by selecting frequencies ω_0 accomplishing the additional condition of an almost perfect matching of impedance with that of air. In other words, $Z_m^2(\omega_0) = \rho_m(\omega_0)B_m(\omega_0) \approx \rho_b B_b = Z_b^2$. A inspection of Fig. 4 shows that this condition occurs at frequencies where both metamaterial parameters are negative and $\rho_m \approx 1/B_m$.

Both conditions allow the phenomenon of tunneling through a narrow channel existing in the DNZ metamaterial, as shown in Fig. 9(b). This figure shows a snapshot of the transmission of a sound wave with frequency 0.1455 (in reduced units) through a metamaterial slab with an embedded narrow channel determined by a perfect rigid wall, which is represented by the white stripe. The slab is made of nine layers and the channel is one lattice parameter wide along the vertical y direction and R_b being its thickness along the x direction. Note that a is the minimum length of the channel that can be constructed with the metamaterial under study. For comparison purposes, Fig. 9(a) shows the result using the same configuration except that the DNZ metamaterial has been removed from the channel. As observed, part of the incident wave is reflected by the rigid wall while the transmitted wave no longer has a plane wave front.

It is interesting to point out that the behavior characterized in Fig. 9(b) has been obtained in the frequency region where the metamaterial is double negative. In order to check the
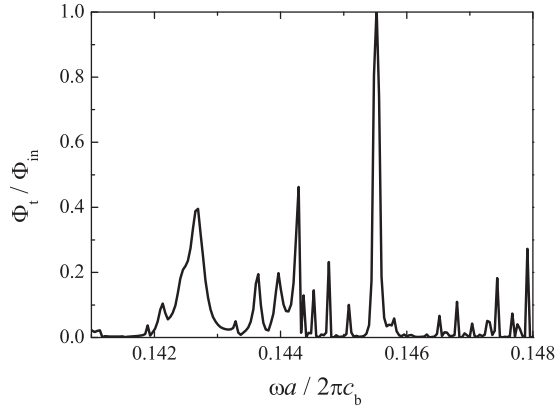
FIG. 10. Calculated transmitted energy flux through the metamaterial slab shown in Fig. 9(b). Values are obtained in a frequency range where the metamaterial is double negative (see Fig. 4). Unity transmission is produced at 0.1455 where the tunneling effect occurs.

perfect transmission of the sound energy we have calculated the transmitted energy flux, Φ_t, and have compared it with the impinging energy flux, Φ_{in}.

Figure 10 shows the transmitted energy flux normalized to the incoming flux. The energy flux passing through a surface S at an arbitrary position x is calculated using the expression,

$$\Phi(x) = \int_S \mathrm{Re}(P v_x^* \cdot dS_x), \qquad (11)$$

where S_x is the area perpendicular to the x axis, v_x^* the complex conjugate of the velocity x component, and P the pressure field. It is noticeable that perfect transmission is obtained at 0.1455, the frequency at which one snapshot of the tunneling effect is represented in Fig. 9. Note that the tunneling appears at a frequency corresponding to a wavelength much larger than the channel thickness a, i.e., at $\lambda \approx 6.9a$. Also note that tunneling at larger wavelengths in comparison with the channel aperture can be obtained by simply using metamaterials based on a larger cavity length L since the DNZ behavior is obtained at lower frequencies.

The numerical simulation in Fig. 9(b) along with the calculated unity transmission obtained at the same frequency confirm that "squeezed acoustic waves" will tunnel with a negligible phase shift through extremely narrow DNZ channels based on the structures introduced here. Recently, Fleury and Alù have theoretically proposed that extraordinary sound transmission through DNZ ultranarrow channels is also possible by loading a capillarity tube with membranes.[40]

B. Controlling the radiation field

A recent work by Wei and co-workers[41] theoretically investigated the propagation in 2D index-near-zero (INZ) and DNZ acoustic metamaterials embedded with defects. They did not propose any artificial structure for observing the properties they claimed, but their simulations indicate that total transmission, total reflection, and tunable transmission are indeed possible by introducing appropriate defects. Particularly, they show that acoustic cloaking was indeed possible. Similar results can also be obtained using our proposed artificial structures by selecting the frequencies at which INZ and
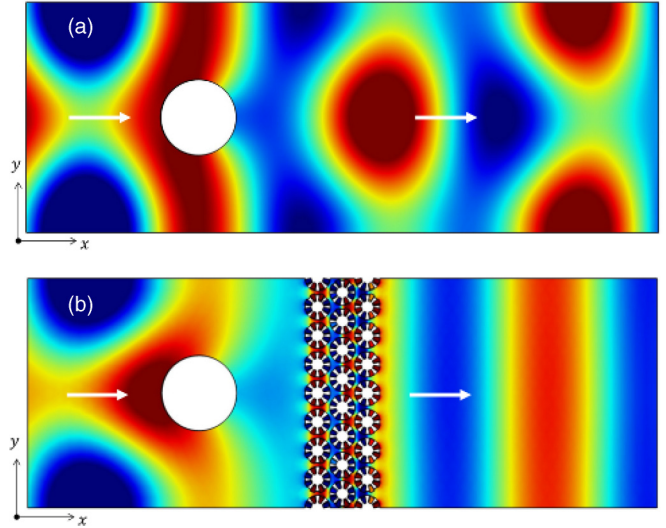
FIG. 11. (Color online) (a) Calculated map of the pressure field (real part) for the scattering of a sound wave with an acoustically rigid cylinder (white circle). (b) Map for the case in which a DNZ metamaterial slab is placed behind the cylinder. The white arrows represent the direction of sound propagation. It is shown that the higher order modes resulting from the scattering with the cylinder are completely suppressed by the DNZM slab.

DNZ take place. However, in this section, we report another interesting application of DNZ metamaterials: the control of the radiation pattern by a DNZ metamaterial slab.

Let us consider the scattering of a plane wave impinging on a defect embedded in an empty 2D waveguide. For simplification purposes we consider that the defect is a rigid scatterer with circular section and radius R_d. The scattered field has a complex pattern which is shown in Fig. 11(a). Note that the radiation field contains plane waves with orders higher than zero. However, if we place a slab of our DNZ material at a certain distance behind the rigid scatterer the plane wave front is perfectly recovered. This phenomenon is observed in Fig. 11(b), which shows a snapshot of the total pressure for the systems described. A similar effect was described by Alù and co-workers[39] studying the propagation of EM waves in ENZ materials. The reason for this similarity is the formal equivalence between the wave equation representing the propagation for EM waves with phase velocity being infinitely large (i.e., $\nabla^2 E = 0$) with that for acoustic waves also accomplishing the condition of infinitely large phase velocity, $\nabla^2 P = 0$.

Note that the DNZ material is made of just three layers of our artificial structures. The plot demonstrated how the complex radiation pattern impinging the DNZ slab is transformed at the exit side, the radiation field being conformal with the exit metamaterial surface due to the small phase variation inside the material. Since all the points at the exit surface start emitting at the same time, the resulting wave front will keep the shape of the surface, which in our example is a plane. In this way, we have filtered all off-normal components of the impinging wave.

In spite of the simplifications employed for the scatterer shape defining the defect and its acoustic properties, the main
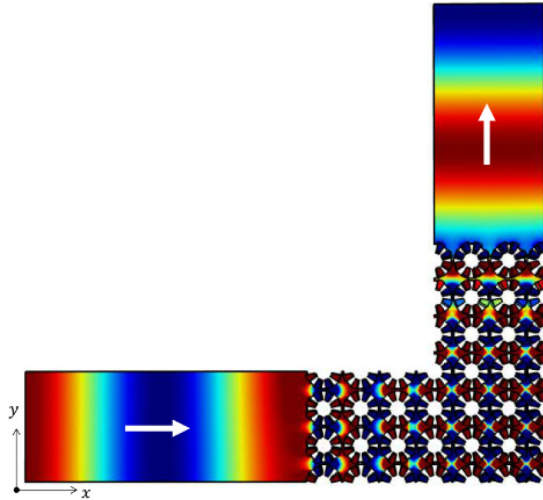
FIG. 12. (Color online) Snapshot of the pressure field (real part) showing the transmission through a 90° bend. The plot shows unity transmission through the bend which has a DNZ metamaterial embedded at the corner.

conclusion is completely general and can be extended to any other shapes and material composition of the scatterer. In fact, this result can be considered as an application of the DNZ materials as media for tailoring the phase of radiation pattern of arbitrary sources, an application that has been reported for ENZ materials.[39]

C. Perfect transmission through sharp bends and corners

The idea of tunneling of EM waves through narrow channels embedded in a ENZ material can be extended to the case in which the ENZ material form sharp bends and corners.[36] As in the case of perfect transmission through narrow channels, the extremely large value of the wavelength inside the ENZ material implies that the wave must be able to propagate with negligible reflection losses at abrupt bends or junctions.[42]

In the acoustic counterpart, the DNZ materials can be employed as the media allowing perfect sound transmission inside 2D waveguides with sharp bends and corners. As an example, we studied the case of two perpendicular waveguides with equal thicknesses.

Figure 12 represents the pressure transmission through a 90° bend in which thickness of the horizontal and vertical arms is $3a$, with a being the lattice period. Note that the sound wave passes through the corner without reflection, keeping its plane wave front. The EM counterpart of this phenomenon has been experimentally demonstrated using ENZ materials by Edwards and co-workers.[43]

D. Acoustic waveguide splitter

Aside from applications based on a single waveguide, DNZ metamaterials also allow the design of networks containing more than two ports. A representative example consists of a waveguide splitter, where the energy of an input signal is divided into multiple outputs. This kind of device has been recently proposed for EM waves, showing that it can provide a perfect distribution of power regardless of its shape and
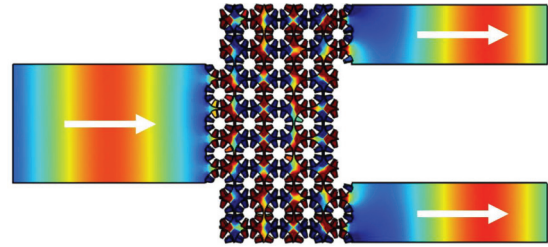
FIG. 13. (Color online) Pressure map of a power divider based on a DNZ metamaterial. The energy of the input port is transferred to the output waveguides. The white arrows indicate the direction of sound propagation.

cross section, as well as the number of outputs and their orientations.[44] Note that these features are achieved provided that the sum of the cross sections of all outputs equals that of the input port.

Figure 13 shows an example of waveguide divider where the energy of the input port (left port) is transferred to two outputs (right ports). The thickness of the input port is $6a$, each output being $3a$ thick. The operating frequency and the geometrical parameters of the arrangement is the same as the previous section. Since there is perfect transmission of energy, no reflections are observed at the input while the amplitude of the outgoing waves matches to that of the incident wave. Note that this device can also be used in a reverse way, in such a manner that it works as a combiner. If both right ports are simultaneously excited their energy will be transmitted towards the left access.

V. EXPERIMENTS AND DISCUSSION

A first attempt for the experimental verification of the proposed structures is reported here. We have fabricated two samples made out of plastic using a 3D printer, which appears acoustically rigid with respect to air. Figure 14 shows photographs of both samples, both of which are fabricated in a single piece including the cylindrical scatterers, the bottom surface of the 2D waveguide, and the two side walls.

Sample A consists of seven rows of structured scatterers with parameters (see Fig. 1): $R_b = 9.2$ mm, $R_a = R_b/2$, $h = 9$ mm, $L = 3.5h$, and $\alpha = \pi/8$. They were distributed on a hexagonal lattice with lattice constant $a = 21$ mm, the corresponding filling fraction being 70%. Sample B, which is shown in Fig. 14(b), is fabricated with smaller scatterers ($R_b = 7$ mm), the resulting filling fractions being 40%. The length of the cavities drilled in the waveguide bottom [see Fig. 1(b)] are $L = 3.5h$ and $L = 2.5h$ for sample A and sample B, respectively. The sample thickness is determined by the number of rows while their width corresponds to one lattice parameter a, in such a manner that the lateral walls act as mirrors. Therefore, the samples can be considered as infinitely extended clusters along the lateral sides.

The waveguide where impinging and transmitted waves propagate consists of an aluminum tube with height h and width a. A sample holder has been milled in the middle part, leaving 1.5 m of waveguide at each side. In one side of the tube a speaker is placed to provide an excitation signal and a microphone B&K 4958 is located at the other side of the
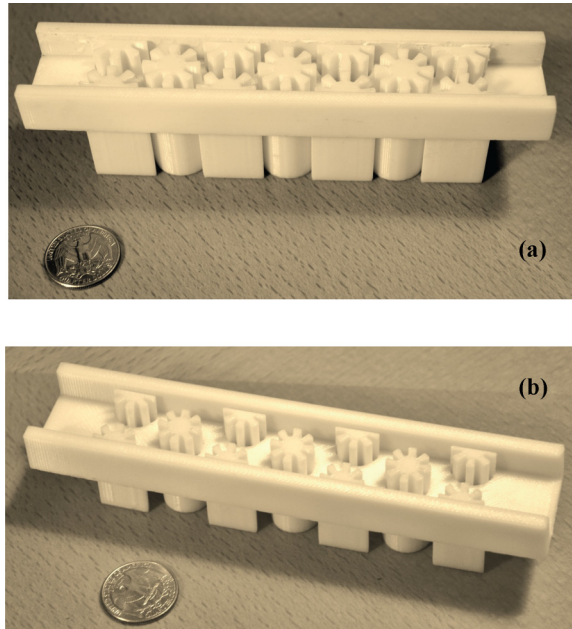
FIG. 14. (Color online) Photographs of the samples fabricated with a 3D printer. The scattering units are distributed in a hexagonal lattice with equal lattice constant ($a = 21$ mm), but with different external radius: (a) $R_b = 9.2$ mm for sample A, and (b) $R_b = 7$ mm for sample B. The filling fraction of the underlying lattices are 70% and 40%, respectively.

FIG. 15. (Color online) (a) Frequency dependence of the measured (symbols) and calculated (continuous lines) transmittance for sample A with $L = 31.5$ mm. (b) Results for sample B with $L = 22.5$ mm. The calculations have been performed using an algorithm based on the FEM. The shadowed regions define the frequencies where acoustic parameters take negative values according to the homogenization theory. The unity transmission peaks correspond to frequencies where the samples behave as a double negative material.

sample at a distance of 20 cm with respect to the center of the sample. It is worth noting that the waveguide has a finite length and, therefore, unwanted reflections take place at both ends. To avoid this issue we have employed a pulsed measure technique. In brief, this technique uses as an exciting signal a short chirp containing all the frequencies of interest, and meanwhile the data are acquired by the microphone until the time when the first echo arrives. This process is performed several times and the average value of the pressure is processed in order to improve the signal-to-noise ratio.

The characterization of the samples has been carried out in terms of their transmission properties. First, the frequency dependence of the transmitted pressure P_t is measured by acquiring the pressure field for each sample. Then a reference pressure P_0 is obtained through a similar measurement where the sample holder is covered by a piece which gives the form of an empty waveguide. Thus, the insertion losses are calculated as $IL = P_0/P_t$. Figure 15 shows the measured data compared with the inverse of the transmission coefficient obtained from finite element simulations. As shown, both structures present a band gap characterized by a high attenuation profile. It is important pointing out that high losses were experimentally observed in the whole spectrum, even for the case of an empty waveguide. These losses are due to the small dimensions of the waveguide, in such a manner that energy is dissipated by viscous friction in the walls of the waveguide and the sample. Because of this the transmission peak due to double negative propagation could not be experimentally detected. Nevertheless, the positions of band gaps corresponding to frequencies where our artificial structures dynamically answer like single-negative materials are positively characterized. This

agreement is encouraging, since negative dynamical mass in air were only obtained by man-made structures based on membranes.[21] Structures with larger dimensions, operating at lower frequencies, are expected to decrease the viscous losses and phenomena associated to double negativity and DNZ behaviors hopefully will be observed.

VI. SUMMARY AND CONCLUSIONS

In summary, we have introduced quasi-2D artificial structures based on building units that are angularly anisotropic. The effective parameters obtained from a homogenization theory based on multiple scattering indicates that they can be tailored by adjusting the parameter of the building units. For the units analyzed here we demonstrated that the metameterials show single-negative behavior, double negative behavior, and DNZ behavior depending on the frequency region. In particular, we have theoretically demonstrated that at the frequencies with negative mass density, our structures can be used for amplification of acoustic evanescent modes and therefore for the possible realization of devices for acoustic superlensing. Moreover, in the frequencies with DNZ behavior we have also shown that they can be used for devices for squeezing the acoustic waves through extremely narrow channels, like filters of transverse modes and for the perfect transmission trough sharp bends and corners.

However, a word of caution should be mentioned about losses in the acoustic metamaterials. While our experiments with the fabricated samples have shown their negative mass behavior at kHz frequencies, the double negative behavior expected in both samples was completely hidden by the strong sound absorption in that range of frequencies. Since

the constituent materials have nonintrinsic losses, the strong attenuation observed is attributed to viscous losses in air that are probably enhanced by the fact that sound propagating within the double negative band has a very low group velocity. It is concluded that the practical realization of the metamaterials here proposed should be done with larger dimensions where the viscous losses are expected to be smaller.

ACKNOWLEDGMENTS

APPENDIX: T MATRIX OF AN ANISOTROPIC CYLINDER LOCATED INSIDE IN A 2D WAVEGUIDE

This appendix describes how the mode-matching method is applied to obtain the T matrix of the metamaterial building units shown in Figs. 1(a)–1(b).

The derivation of the T matrix of an isolated scatterer embedded in a 2D waveguide starts by dividing the space inside the 2D waveguide in two regions: Region I corresponds to the space outside the scatterer ($r > R_b$) and region II defines the space inside the scatterer ($R_a < r < R_b$). The pressure field in region I can be written as a sum of linear combinations of solutions of the empty cavity,

$$P^I(r,\theta,z;\omega) = \sum_{n=0}^{\infty} \sum_{q=-\infty}^{\infty} \left[A_{qn} J_q(k_n^I r) + B_{qn} H_q(k_n^I r) \right]$$
$$\times e^{iq\theta} \Phi_n^I(z), \quad \text{(A1)}$$

where the coefficients A_{qn} and B_{qn} represent the incident and scattered pressure fields, respectively. $\Phi_n^I(z)$ are normalized functions accomplishing the condition that the normal velocity is zero at the bottom and top surface walls, i.e., $\frac{\partial \Phi_n^I(z)}{\partial z} = 0$ at $z = 0$ and $z = h$, respectively. In other words,

$$\Phi_n^I(z) = \sqrt{\frac{\epsilon_n}{h}} \cos\left(\frac{n\pi}{h}z\right), \quad \epsilon_n = \begin{cases} 1 & if \quad n = 0, \\ 2 & if \quad n \neq 0. \end{cases} \quad \text{(A2)}$$

Finally, k_n^I in Eq. (A1) is the transverse wave number,

$$k_n^I = \sqrt{\left(\frac{\omega}{c_b}\right)^2 - \left(\frac{n\pi}{h}\right)^2}, \quad \text{(A3)}$$

where n is an integer with values $n = 0, 1, \ldots, \infty$.

In region II ($R_b < r < R_a$) the pressure can be expressed as

$$P^{II}(r,\theta;\omega) = \sum_{m=0}^{\infty} \sum_{q=-\infty}^{\infty} C_{qm} \left[J_0(k_m^{II} r) \right.$$
$$\left. - \frac{\dot{J}_0(k_m^{II} R_a)}{\dot{Y}_0(k_m^{II} R_a)} Y_0(k_m^{II} r) \right] e^{iq\theta} \Phi_m^{II}(z), \quad \text{(A4)}$$

where the dot on top of the Bessel functions indicates the derivative with respect to the argument; i.e., $\dot{J}_0(x) = \frac{\partial J_0(x)}{\partial x}$. Similarly, $\Phi_m^{II}(z)$ being the normalized functions

$$\Phi_m^{II}(z) = \sqrt{\frac{\epsilon_m}{h+L}} \cos\left(\frac{m\pi}{h+L}z\right), \quad \text{(A5)}$$

and the transverse wave number is now

$$k_m^{II} = \sqrt{\left(\frac{\omega}{c_s}\right)^2 - \left(\frac{m\pi}{h+L}\right)^2}, \quad m = 0, 1, \ldots, \infty. \quad \text{(A6)}$$

Note that the function P^{II} satisfies the boundary condition $\partial P^{II}/\partial r = 0$ (at $z = 0, h + L$), and also verifies the boundary condition at the surface of the rigid cylinder $r = R_a$. In fact, the expression P^{II} corresponds to the case of an anisotropic metafluid having a coefficient of anisotropy $\gamma = 0$ (no anisotropy) as discussed by Spiousas *et al.*,[6] who concluded that $\gamma = 0$ is valid for wavelengths much larger than the width of the angular sectors[6]; i.e., for $\lambda \gg d = \alpha R_b$. In other words, the Bessel function $J_{\gamma q}$ should appear instead for structures where $\gamma \neq 0$.

The coefficients C_m and B_{qn} are obtained by imposing the boundary conditions at the scatterer surface, $r = R_b$. The first condition is the continuity of the pressure fields P^I and P^{II}. The fields at the boundary surfaces are projected on the waveguide modes through an integration from $z = 0$ to h:

$$\int_0^h P^I(r,\theta,z)|_{r=R_b} \Phi_k^I(z) dz$$
$$= \int_0^h P^{II}(r,\theta,z)|_{r=R_b} \Phi_k^I(z) dz. \quad \text{(A7)}$$

On the other hand, the continuity of the normal component of the sound speed is obtained by projecting it at the boundary surface on the waveguide modes of the cavity. Therefore,

$$\frac{1}{\rho_b} \int_0^{h+L} \frac{\partial P^I(r,\theta,z)}{\partial r}|_{r=R_b} \Phi_k^{II}(z) dz$$
$$= \frac{1}{\rho_s} \int_0^{h+L} \frac{\partial P^{II}(r,\theta,z)}{\partial r}|_{r=R_b} \Phi_k^{II}(z) dz, \quad \text{(A8)}$$

with ρ_b and ρ_s being the densities of the background and that of the anisotropic cylinder, respectively. The density ρ_s is
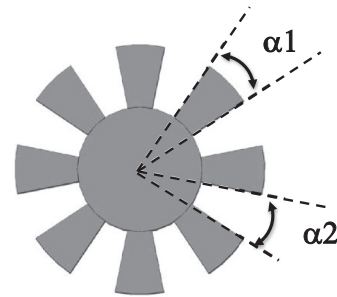
FIG. 16. Section of a general scatterer in which the solid sectors (gray regions defined by angles α_1) have different area than the air sectors (white regions defined by angles α_2).

calculated using the expression[6]

$$\rho_s = \frac{\alpha_1 + \alpha_2}{\alpha_2} \rho_b, \tag{A9}$$

where α_1 and α_2 are the angles describing the generalized scatterer shown in Fig. 16.

After integrating and taking into account the orthogonality properties of the normalized functions $\Phi_n^I(z)$ and Φ_m^{II}, Eqs. (A7) and (A8) become, respectively,

$$A_{qk} J_q(k_k^I R_b) + B_{qk} H_q(k_k^I R_b) = \sum_{m=0}^{\infty} C_{qm} \left[J_0(k_m^{II} R_b) - \frac{\dot{J}_0(k_m^{II} R_a)}{\dot{Y}_0(k_m^{II} R_a)} Y_0(k_m^{II} R_b) \right] G_{km}, \tag{A10}$$

and

$$\frac{1}{\rho_b} \sum_{n=0}^{\infty} \left[A_{qn} \dot{J}_q(k_n^I R_b) + B_{qn} \dot{H}_q(k_n^I R_b) \right] k_n^I G_{nk} = \frac{k_k^{II}}{\rho_s} C_{qk} \left[\dot{J}_0(k_k^{II} R_b) - \frac{\dot{J}_0(k_k^{II} R_a)}{\dot{Y}_0(k_k^{II} R_a)} \dot{Y}_0(k_k^{II} R_b) \right]. \tag{A11}$$

The coefficients C_{qk} obtained from Eq. (A11) are

$$C_{qk} = \frac{\rho_s}{\rho_b} \sum_{n=0}^{\infty} \frac{k_n^I}{k_k^{II}} \left[\frac{\dot{J}_q(k_n^I R_b) G_{nk}}{\dot{J}_0(k_k^{II} R_b) - \frac{\dot{J}_0(k_k^{II} R_a)}{\dot{Y}_0(k_k^{II} R_a)} \dot{Y}_0(k_k^{II} R_b)} A_{qn} + \frac{\dot{H}_q(k_n^I R_b) G_{nk}}{\dot{J}_0(k_k^{II} R_b) - \frac{\dot{J}_0(k_k^{II} R_a)}{\dot{Y}_0(k_k^{II} R_a)} \dot{Y}_0(k_k^{II} R_b)} B_{qn} \right]. \tag{A12}$$

These coefficients are inserted in Eq. (A10) to obtain, after some algebra, the following relation:

$$A_{qk} J_q(k_k^I R_b) - \frac{\rho_s}{\rho_b} \sum_{m=0}^{\infty} \sum_{n=0}^{\infty} \dot{J}_q(k_n^I R_b) G_{km} G_{nm} \frac{J_0(k_m^{II} R_b) - \frac{\dot{J}_0(k_m^{II} R_a)}{\dot{Y}_0(k_m^{II} R_a)} Y_0(k_m^{II} R_b)}{\dot{J}_0(k_m^{II} R_b) - \frac{\dot{J}_0(k_m^{II} R_a)}{\dot{Y}_0(k_m^{II} R_a)} \dot{Y}_0(k_m^{II} R_b)} \frac{k_n^I}{k_m^{II}} A_{qn}$$

$$= - \left[B_{qk} H_q(k_k^I R_b) - \frac{\rho_s}{\rho_b} \sum_{m=0}^{\infty} \sum_{n=0}^{\infty} \dot{H}_q(k_n^I R_b) G_{km} G_{nm} \frac{J_0(k_m^{II} R_b) - \frac{\dot{J}_0(k_m^{II} R_a)}{\dot{Y}_0(k_m^{II} R_a)} Y_0(k_m^{II} R_b)}{\dot{J}_0(k_m^{II} R_b) - \frac{\dot{J}_0(k_m^{II} R_a)}{\dot{Y}_0(k_m^{II} R_a)} \dot{Y}_0(k_m^{II} R_b)} \frac{k_n^I}{k_m^{II}} B_{qn} \right]. \tag{A13}$$

This equation can be rewritten in matrix form as

$$\sum_m (H_q)_{km} B_{qm} = \sum_n (J_q)_{kn} A_{qn}, \tag{A14}$$

with

$$(J_q)_{kn} \equiv J_q(k_n^I R_b) \delta_{kn} - \frac{\rho_s}{\rho_b} \sum_m \dot{J}_q(k_n^I R_b) G_{km} G_{nm} \frac{J_0(k_m^{II} R_b) - \frac{\dot{J}_0(k_m^{II} R_a)}{\dot{Y}_0(k_m^{II} R_a)} Y_0(k_m^{II} R_b)}{\dot{J}_0(k_m^{II} R_b) - \frac{\dot{J}_0(k_m^{II} R_a)}{\dot{Y}_0(k_m^{II} R_a)} \dot{Y}_0(k_m^{II} R_b)} \frac{k_n^I}{k_m^{II}}, \tag{A15}$$

$$(H_q)_{kn} \equiv - \left[H_q(k_n^I R_b) \delta_{kn} - \frac{\rho_s}{\rho_b} \sum_m \dot{H}_q(k_n^I R_b) G_{km} G_{nm} \frac{J_0(k_m^{II} R_b) - \frac{\dot{J}_0(k_m^{II} R_a)}{\dot{Y}_0(k_m^{II} R_a)} Y_0(k_m^{II} R_b)}{\dot{J}_0(k_m^{II} R_b) - \frac{\dot{J}_0(k_m^{II} R_a)}{\dot{Y}_0(k_m^{II} R_a)} \dot{Y}_0(k_m^{II} R_b)} \frac{k_n^I}{k_m^{II}} \right], \tag{A16}$$

where

$$G_{nm} = \frac{1}{2} \sqrt{\frac{h}{h+L}} \epsilon_n \epsilon_m \left[\operatorname{sinc}\left((k_{zn}^I + k_{zm}^{II})h\right) + \operatorname{sinc}\left((k_{zn}^I - k_{zm}^{II})h\right) \right]. \tag{A17}$$

Since the T matrix is defined as the relation between the scattering coefficients B_{qn} and that of the incident field A_{qn},

$$B_{qm} = \sum_n (T_q)_{mn} A_{qn}, \tag{A18}$$

its matrix elements are quickly derived from Eqs. (A13) and (A14):

$$(T_q)_{mn} = \sum_k (H_q)_{mk}^{-1} (J_q)_{kn}. \tag{A19}$$

*Corresponding author: jsdehesa@upv.es

[1]L. Fok, M. Ambati, and X. Zhang, MRS Bull. **33**, 931 (2008).

[2]R. Craster and S. Guenneau, *Acoustic Metamaterials* (Springer, Berlin, 2013).

[3]J. Li, L. Fok, X. Yin, G. Bartal, and X. Zhang, Nat. Mater. **8**, 931 (2009).

[4]A. Climente, D. Torrent, and J. Sánchez-Dehesa, Appl. Phys. Lett. **97**, 104103 (2010).

[5]T. Martin, M. Nicholas, G. Orris, L. Cai, D. Torrent, and J. Sánchez-Dehesa, Appl. Phys. Lett. **97**, 113503 (2010).

[6]I. Spiousas, D. Torrent, and J. Sánchez-Dehesa, Appl. Phys. Lett. **98**, 244102 (2011).

[7]D. Torrent and J. Sánchez-Dehesa, Phys. Rev. Lett. **103**, 064301 (2009).

[8]D. Torrent and J. Sánchez-Dehesa, New J. Phys. **12**, 073034 (2010).

[9]S. Cummer and D. Schurig, New J. Phys. **9**, 45 (2007).

[10]D. Torrent and J. Sánchez-Dehesa, New J. Phys. **10**, 063015 (2008).

[11]S. Cummer, M. Rahm, and D. Schurig, New J. Phys. **10**, 115025 (2008).

[12]H. Chen and C. Chan, J. Phys. D: Appl. Phys. **43**, 113001 (2010).

[13]A. Garcia-Meca, S. Carloni, C. Barcelo, G. Jannes, J. Sánchez-Dehesa, and A. Martinez, Sci. Rep. **3**, 2009 (2013).

[14]N. Fang, D. Xi, J. Xu, M. Ambati, W. Srituravanich, C. Sun, and X. Zhang, Nat. Mater. **5**, 452 (2006).

[15]S. H. Lee, C. M. Park, Y. M. Seo, Z. G. Wang, and C. K. Kim, J. Phys.: Condens. Matter **21**, 175704 (2009).

[16]J. Fey and W. M. Robertson, J. Appl. Phys. **109**, 114903 (2011).

[17]V. M. García-Chocano, R. Graciá-Salgado, D. Torrent, F. Cervera, and J. Sánchez-Dehesa, Phys. Rev. B **85**, 184102 (2012).

[18]Z. Liu, X. Zhang, Y. Mao, Y. Zhu, Z. Yang, C. Chan, and P. Sheng, Science **289**, 1734 (2000).

[19]Z. Yang, J. Mei, M. Yang, N.H. Chan, and P. Sheng, Phys. Rev. Lett. **101**, 204301 (2008).

[20]S. Yao, X. Zhou, and G. Hu, New J. Phys. **12**, 103025 (2010).

[21]C. M. Park, J. J. Park, S. H. Lee, Y. M. Seo, C. K. Kim, and S. H. Lee, Phys. Rev. Lett. **107**, 194301 (2011).

[22]J. Li and C. T. Chan, Phys. Rev. E **70**, 055602 (2004).

[23]Y. Ding, Z. Liu, C. Qiu, and J. Shi, Phys. Rev. Lett. **99**, 093904 (2007).

[24]Y. Cheng, J. Y. Xu, and X. J. Liu, Phys. Rev. B **77**, 045134 (2008).

[25]S. H. Lee, C. M. Park, Y. M. Seo, Z. G. Wang, and C. K. Kim, Phys. Rev. Lett. **104**, 054301 (2010).

[26]L. Fok and X. Zhang, Phys. Rev. B **83**, 214304 (2011).

[27]Z. Liang and J. Li, Phys. Rev. Lett. **108**, 114301 (2012).

[28]Y. Xie, B.-I. Popa, L. Zigoneanu, and S. A. Cummer, Phys. Rev. Lett. **110**, 175501 (2013).

[29]R. Graciá-Salgado, D. Torrent, and J. Sánchez-Dehesa, New J. Phys. **14**, 103052 (2012).

[30]D. Torrent, A. Håkansson, F. Cervera, and J. Sánchez-Dehesa, Phys. Rev. Lett. **96**, 204302 (2006).

[31]D. Torrent and J. Sánchez-Dehesa, New J. Phys. **13**, 093018 (2011).

[32]R. Gracia-Salgado, D. Torrent, and J. Sanchez-Dehesa, New J. Phys. **14**, 103052 (2012).

[33]M. Ambati, N. Fang, C. Sun, and X. Zhang, Phys. Rev. B **75**, 195447 (2007).

[34]A. Alù and N. Engheta, Phys. Rev. E **72**, 016623 (2005).

[35]Y. Wu and J. Li, Appl. Phys. Lett. **102**, 183105 (2013).

[36]M. Silveirinha and N. Engheta, Phys. Rev. Lett. **97**, 157403 (2006).

[37]R. Liu, Q. Cheng, T. Hand, J.J. Mock, T. J. Cui, S. A. Cummer, and D. R. Smith, Phys. Rev. Lett. **100**, 023903 (2008).

[38]B. Edwards, A. Alù, M. E. Young, M. Silveirinha, and N. Engheta, Phys. Rev. Lett. **100**, 033903 (2008).

[39]A. Alù, M.G. Silveirinha, A. Salandrino, and N. Engheta, Phys. Rev. B **75**, 155410 (2007).

[40]R. Fleury and A. Alù, Phys. Rev. Lett. **111**, 055501 (2013).

[41]Y. Wei, Y. Cheng, and X.-J. Liu, Appl. Phys. Lett. **102**, 174104 (2013).

[42]J. Luo, P. Xu, H. Chen, B. Hou, L. Gao, and Y. Lai, Appl. Phys. Lett. **100**, 221903 (2012).

[43]B. Edwards, A. Alu, M. Silveirinha, and N. Engheta, J. Appl. Phys. **105**, 044905 (2009).

[44]A. Ourir, A. Maurel, and V. Pagneux, Opt. Lett. **38**, 2092 (2013).